7-1-2000

Optical properties of bulk and thin-film $SrTiO_3$ on Si and Pt

Stefan Zollner
Motorola Semiconductor Products Sector, Mesa, Arizona

A. A. Demkov
Motorola Semiconductor Products Sector, Mesa, Arizona

R. Liu
Motorola Semiconductor Products Sector, Mesa, Arizona

P. L. Fejes
Motorola Semiconductor Products Sector, Mesa, Arizona

R.B. Gregory
Motorola Semiconductor Products Sector, Mesa, Arizona

See next page for additional authors

Optical properties of bulk and thin-film $SrTiO_3$ on Si and Pt

Stefan Zollner,[a] A. A. Demkov, R. Liu, P. L. Fejes, R. B. Gregory, and Prasad Alluri
Motorola Semiconductor Products Sector, MD M360, 2200 West Broadway Road, Mesa, Arizona 85202

J. A. Curless, Z. Yu, J. Ramdani, and R. Droopad
Motorola Physical Sciences Research Laboratories, Tempe, Arizona 85284

T. E. Tiwald, J. N. Hilfiker, and J. A. Woollam
J. A. Woollam Company, 645 M Street, Suite 102, Lincoln, Nebraska 68508

(Received 17 January 2000; accepted 5 April 2000)

We have studied the optical properties (complex dielectric function) of bulk $SrTiO_3$ and thin films on Si and Pt using spectroscopic ellipsometry over a very broad spectral range, starting at 0.03 eV [using Fourier transform infrared (FTIR) ellipsometry] to 8.7 eV. In the bulk crystals, we analyze the interband transitions in the spectra to determine the critical-point parameters. To interpret these transitions, we performed band structure calculations based on *ab initio* pseudopotentials within the local-density approximation. The dielectric function was also calculated within this framework and compared with our ellipsometry data. In the FTIR ellipsometry data, we notice a strong lattice absorption peak due to oxygen-related vibrations. Two longitudinal optic (LO) phonons were also identified. In $SrTiO_3$ films on Si, the refractive index below the band gap decreases with decreasing thickness because of the increasing influence of the amorphous interfacial layer between the $SrTiO_3$ film and the Si substrate. There is also a decrease in amplitude and an increase in broadening of the critical points with decreasing thickness. In $SrTiO_3$ films on Pt, there is a strong correlation between the crystallinity and texture of the films (mostly aligned with the Pt pseudosubstrate) and the magnitude of the refractive index, the Urbach tail below the bulk band edge, and the critical-point parameters. FTIR reflectance measurements of $SrTiO_3$ on Pt (reflection–absorption spectroscopy) show absorption peaks at the LO phonon energies, a typical manifestation of the Berreman effect for thin insulating films on a metal. The Urbach tail in our ellipsomety data and the broadening of the optical phonons in $SrTiO_3$ on Pt are most likely caused by oxygen vacancy clusters. [S0734-211X(00)00904-5]

I. INTRODUCTION

Oxides with perovskite crystal structure, such as $SrTiO_3$, are important candidates for ultrathin gate dielectrics or capacitors (replacing SiO_2 and silicon nitrides) in microelectronics because of their large dc dielectric constant, or permittivity,[1] ϵ_0. $SrTiO_3$ can be grown epitaxially on Si (001), with its unit cell rotated by 45° with respect to the underlying Si substrate, resulting in a lattice mismatch of only 1.7%. Equivalent gate oxide thicknesses on the order of 10 Å with low leakage currents have been achieved.[2–6] When $SrTiO_3$ is deposited directly on Si, an amorphous nonstoichiometric interfacial layer (10–30 Å thick) is usually formed during the later stages of growth, except when the $SrTiO_3$ film is very thin.[2,6] This is undesirable, since it reduces the specific capacitance. Optical tools like spectroscopic ellipsometry can easily be adapted for in-line or *in situ* diagnostics of $SrTiO_3$ on Si, therefore understanding the optical properties of such thin films is important.

Whenever we are interested in the properties of thin films, it is usually a good idea to start with studying the bulk, both theoretically and experimentally (see Sec. II). Following Jellison *et al.*,[7] we measured the dielectric function ϵ of bulk $SrTiO_3$ from 0.03 to 8.7 eV. In comparison with *ab initio* band structure calculations based on the local density approximation using a plane wave basis set, we identify critical points in the spectra due to optical interband transitions from the (primarily) $O(2p)$ valence band to the $Ti(3d)$ conduction band at various regions in the Brillouin zone. We also study the lattice vibrations of $SrTiO_3$ by Fourier transform (FTIR) ellipsometry.

After the completion of this initial step, we discuss the optical properties of $SrTiO_3$ films grown on Si (Sec. III) and Pt (Sec. IV). We compare with data for $SrTiO_3$ films on MgO grown by molecular beam epitaxy (MBE).[7] In particular, we correlate the dielectric functions of $SrTiO_3$ films with structural properties, such as thickness and stoichiometry, crystal quality, grain size and texture in polycrystalline films, and oxygen vacancies.

II. OPTICAL PROPERTIES OF BULK $SrTiO_3$

A. Experimental procedure and results

Two bulk $SrTiO_3$ crystals, (100) oriented and $10\times10\times0.5$ mm in size, were obtained commercially from Princeton Scientific Corporation. One piece was polished on both sides (for transmission measurements), the other one on only

[a]Corresponding author; electronic mail: Stefan.Zollner@motorola.com

one side (for reflection ellipsometry). We followed the procedure of Jellison and co-workers[7] to determine the dielectric function ϵ of $SrTiO_3$ from 0.74 to 8.7 eV.

The ellipsometric angles ψ and Δ were acquired from 0.74 to 6.6 eV in 0.01 eV steps at three angles of incidence (65°, 70°, and 75°) on a Woollam VASE ellipsometer with vertical sample mounting. Our rotating-analyzer instrument uses a computer-controlled MgF_2 Berek waveplate as a compensator to improve the accuracy of the ellipsometric angles, particularly below the onset of direct absorption (at about 3.5 eV). Tests on standard samples, such as a Si substrate, indicate that the accuracy of our commercial instrument approaches or exceeds that of Jellison's two-channel polarization modulation ellipsometer,[8,9] but exceeds its spectral range (1.48–5.3 eV). For an insulator near the band gap with ϵ_1 on the order of 5–10, absorption coefficients of 2000 cm^{-1} and higher can be measured.

We also acquired the ellipsometric angles from 4.25 to 8.7 eV in 0.025 eV steps on the prototype of a commercial vacuum-ultraviolet (VUV) ellipsometer. This rotating-analyzer instrument is also equipped with a MgF_2 compensator. The entire system is purged with dry nitrogen gas to avoid oxygen and water absorption bands and has a fixed angle of incidence of 75.08°. Light from a deuterium lamp passes through a double-chamber Czerny–Turner type monochromator to provide wavelength selection and stray-light rejection. A 0.5 nm bandwidth (25 meV at 8 eV) was achieved by reducing the monochromator slit widths to ensure adequate spectral resolution for the optical features. A photomultiplier tube is used for signal detection.

The deep-UV range above 4 eV is particularly important for large band-gap materials, such as $SrTiO_3$, to reveal the critical points in the spectra, which are related to the quality and composition of the sample. Our experimental data from both instruments are displayed (as a pseudodielectric function) by the dotted line in Fig. 1.

We also measured the transmission of the two-side polished sample in the 1.0–3.4 eV spectral range, using the same VASE ellipsometer in the straight-through configuration at normal incidence. The spectral characteristics of the optical elements (Xe lamp, monochromator, and detector) were taken into account by measuring with and without sample and then normalizing the two spectra. We can measure absorption coefficients between 3 and 150 cm^{-1} with the 0.5 mm thick two-side polished sample, corresponding to transmissions (uncorrected for reflection losses) between 90% and 0.05%, limited by the dynamic range of the Si photodiode used as the detector. The logarithm of the transmission near the band gap is shown as an inset in Fig. 1 (dotted line).

B. Optical constants

It is obvious from Fig. 1 that the imaginary part of the pseudodielectric function ($\langle \epsilon_2 \rangle$) is positive below the band gap of $SrTiO_3$ (around 3.2 eV), where the sample is transparent (see inset). We call this a pseudoabsorption and attribute it to the surface roughness of the sample.[7] It is thus

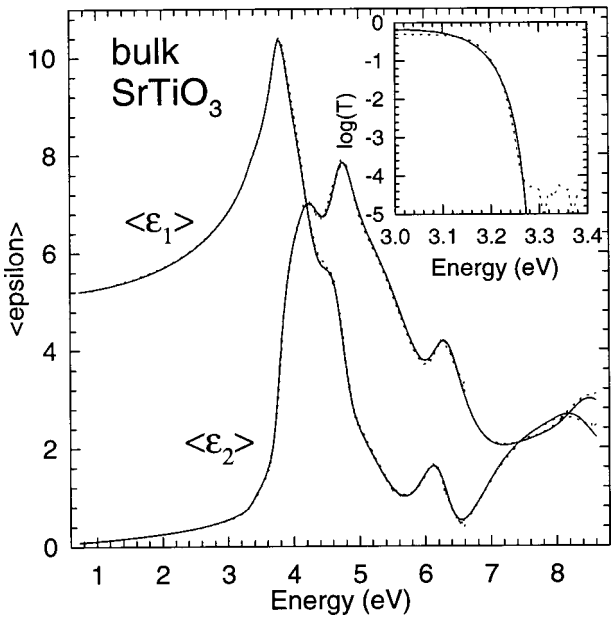

FIG. 1. Pseudodielectric function of bulk $SrTiO_3$ measured using our two ellipsometers to cover the 0.74–8.7 eV photon-energy range (dotted). The inset shows the logarithm of the measured transmission near the band gap (dotted). The solid lines show the data calculated using a model assuming a surface roughness of 24 Å and describing the $SrTiO_3$ optical constants using the Herzinger–Johs parametric oscillator model (Ref. 11) with the parameters given in Table I.

clear that Fig. 1 does not display the *true* dielectric function ϵ of the sample. To determine ϵ of $SrTiO_3$, we simultaneously fit all three data sets in Fig. 1 using a three-phase model (substrate/roughness/ambient). The roughness layer is described within the Bruggeman effective medium theory containing two phases: one with optical properties equal to the substrate (50% volume fraction), the other with optical properties equal to the ambient.[7,10] The optical constants of the $SrTiO_3$ substrate are parametrized using the Herzinger–Johs oscillator model.[11] For the transmission measurement, we also allow roughness on the back surface of the sample. We vary all parameters (those of the oscillator model and the roughness layer thicknesses) until the discrepancy between the model and the data is minimized. The resulting pseudodielectric function and transmission curve are shown by the solid lines in Fig. 1. We find a roughness layer thickness of 24 Å from the ellipsometry spectrum, similar to that of the sample used in Ref. 7 (20 Å). The transmission spectrum is not sensitive to the roughness thicknesses. We set them equal to 24 Å. The parameters of the Herzinger–Johs oscillator model obtained from the fit are given in Table I.

The agreement between our model (solid) and the data (dotted) is excellent (see Fig. 1). There is some difference near the critical points (peaks in the spectra), but it is barely visible. Once we have determined the surface roughness layer thicknesses, we can directly invert our experimental data and find ϵ as a function of photon energy without the need to assume a particular functional form for the dispersion of ϵ. In Fig. 2, we plot the absorption coefficient α determined using this wavelength-by-wavelength fit. There is

TABLE I. Parameters of bulk $SrTiO_3$ for the Herzinger–Johs parametric oscillator model. The first column enumerates the oscillators, the second and third column give the lower (EL) and upper (EU) cutoff of the oscillator with energy EC, amplitude A, and broadening Σ. The remaining columns list the so-called shape parameters describing the lower (L) and upper (U) flanks of the critical points. See Ref. 11 for a detailed description of the parameters.

No.	EL	EU	EC	A	Σ	DISC	L_{pos}	L_{amp}	L_{2d}	U_{pos}	U_{amp}	U_{2d}
0	0	1	3.323	0	50	0	0.5	0.5	0	0.5	0.5	0
1	0	2	3.750	0.253	59	0.015	0.284	0.657	−0.141	0.075	0.086	0.982
2	1	3	4.174	11.518	261	−0.713	0.125	0.017	−1	0.656	0.653	0.729
3	1	4	4.730	9.076	120	0.031	0.243	0.331	−0.308	0.195	0.221	−0.189
4	3	6	6.275	5.664	141	0.076	0.299	0.429	−0.629	0.697	0.312	−0.866
5	4	6	8.424	1.932	306	0.662	0.540	0.343	1	0.366	0	−1
6	6	6	11	167.313	0	0	0.5	0.5	0	0.5	0.5	0

a gap in our data between 3.25 and 3.37 eV, since α between 150 and 2000 cm^{-1} cannot be measured on bulk samples with our setup. Films thinner than 0.5 mm would be needed for such measurements. We partially fill this gap with data by Sata and co-workers,[12] obtained using transmission measurements on thin platelets with a thickness between 60 and 200 μm. The inset of Fig. 2 shows $\sqrt{\alpha}$ near 3.2 eV.

According to Cardona,[13] $SrTiO_3$ has an indirect band gap of about 3.2 eV. This is clearly reflected by the onset of absorption in our data in Fig. 2. A direct gap would lead to a much faster increase of the absorption; see, for example, Fig. 6.15 in Ref. 14 for InSb. Plotting α^2 near 3.2 eV also does not lead to a straight line expected for a direct gap. According to Yu and Cardona[14] (Figs. 6.17–19), plotting $\sqrt{\alpha}$ versus photon energy should result in a stepwise linear behavior related to the various phonons contributing to indirect absorption. This is not observed in our room-temperature data for $SrTiO_3$, possible because of the complicated crystal structure with many phonon modes, some of which are quite low in energy. Nevertheless, we believe that there is an indirect gap with an energy of about 3.1–3.2 eV, but we cannot determine it accurately from room-temperature data. Plotting α^2 in the 3.3–3.6 eV photon-energy range yields a reasonably straight line which crosses the energy axis at roughly 3.4 eV. We thus conclude that there is a direct gap with an energy of about 3.4 eV, just above the indirect gap at about 3.2 eV, which is in good agreement with earlier data.[15,16]

In Fig. 3, we show the dielectric function of bulk $SrTiO_3$ from 0.74 to 8.7 eV (solid lines) calculated from the parametric oscillator model used to fit the experimental data in Fig. 1. A wavelength-by-wavelength fit would result in data not distinguishable from those in Fig. 3. The agreement with the data of Jellison and co-workers[7] in the range of overlap (1.5–5.3 eV) is excellent. The symbols show the data tabulated by Gervais,[17] which were compiled from various sources. The data between 0.9 and 3.0 eV (below the gap)

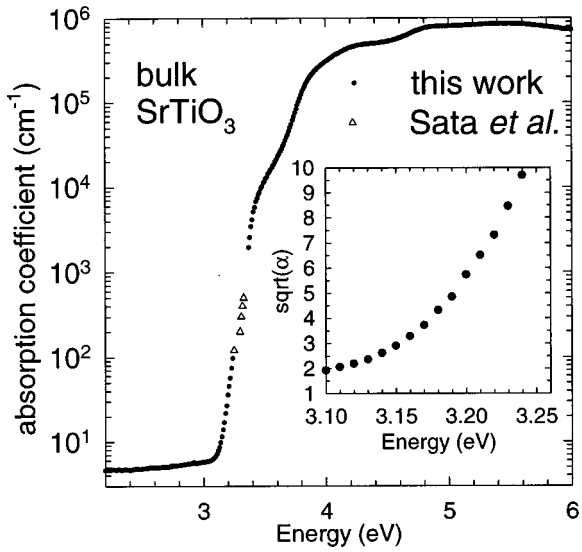

FIG. 2. Semilogarithmic plot of the absorption coefficient α vs photon energy for bulk $SrTiO_3$. The inset shows $\sqrt{\alpha}$ (in units of $cm^{-0.5}$) in the region of the indirect gap (about 3.2 eV). The gap in our data (●) is partially filled by the transmission data of Sata and co-workers (Ref. 12) (△).

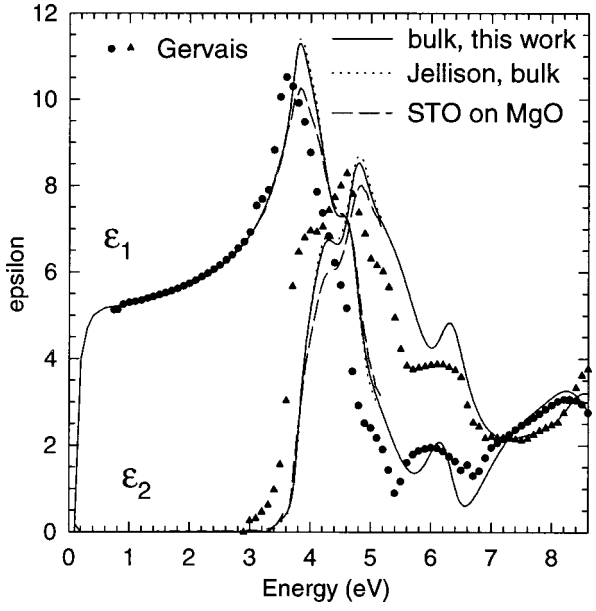

FIG. 3. Dielectric function of bulk $SrTiO_3$ obtained in this work (solid) and in Ref. 7 (dotted) using spectroscopic ellipsometry. Below 0.7 eV, the data were obtained using FTIR ellipsometry. (Symbols) Data from other techniques (Ref. 17). For comparison, the dashed line shows the dielectric function of $SrTiO_3$ on MgO grown by MBE (Ref. 7).

were determined by Cardona[13] using the minimum-deviation prism method, which is the most accurate technique to determine ϵ_1 for a transparent material. Cardona's data are no more than 0.5% higher than those of Ref. 7 and no more than 0.7% larger than ours. Below 0.9 eV, Gervais lists his own data[18] obtained by fitting the infrared spectral region near the lattice absorption using a factorized dielectric response, resulting in ϵ_1 values slightly lower than measured by us. Above the indirect gap, Gervais' data are based on UV reflectivity measurements from 2 to 30 eV combined with a Kramers–Kronig transform.[19] These data are not compatible with ours at all, although there is some resemblance near the critical points. The whole spectrum seems to be shifted toward lower energies and the resolution of the monochromator also may be a problem. The agreement gets better above 6.5 eV.

Simple numerical models are often used for metrology purposes[10] to determine thicknesses of layers (here $SrTiO_3$) on a substrate, such as Si or Pt. A Cauchy model

$$n(\lambda)=n_0+\frac{n_1}{\lambda^2}+\frac{n_2}{\lambda^4} \tag{1}$$

works well in the transparent range below 3 eV (413 nm) with the parameters $n_0=2.281$, $n_1=0.03\,\text{Å}^{-2}$, and $n_2=0.0045\,\text{Å}^{-4}$. A single Lorentz oscillator model

$$\epsilon(E)=\epsilon_\infty+\frac{A}{E_g^2-E^2-i\Gamma E} \tag{2}$$

can be used from 0.74 to 3.4 eV with the parameters $\epsilon_\infty=3.077$, amplitude $A=41.874\,\text{eV}^2$, band gap $E_g=4.466\,\text{eV}$, and broadening $\Gamma=0$. Jellison's Tauc–Lorentz model[20] with a single Lorentz oscillator broadened by an Urbach tail[21] like in amorphous semiconductors can even be used up to 3.5 eV with the following parameters: $\epsilon_\infty=1.668$, amplitude $A=230\,\text{eV}$, broadening $C=1.985\,\text{eV}$, Tauc gap $E_g=3.288\,\text{eV}$, and Lorentz oscillator energy $E_0=4.479\,\text{eV}$. We note that these parameters are not unique. They usually depend strongly on the spectral range to fit the data. Also, they usually carry little physical meaning. No constraints (for example, for ϵ_∞) were applied when fitting these parameters to the measured pseudodielectric function, but the roughness layer (24 Å) was taken into account. Due to the complex critical-point structure of $SrTiO_3$ (see below), using these simple models at higher energies than specified here leads to poor results.

C. Critical points

We have already mentioned that $SrTiO_3$ has an indirect gap at about 3.2 eV and a direct gap of about 3.4 eV. In addition, there are several other structures in the dielectric function at about 3.8, 4.3, 4.8, 6.2, and 8.5 eV. These are van Hove singularities, also known as critical points, related to optical interband transitions from the highest valence bands to the lowest conduction bands at various regions in the Brillouin zone.[14] To study these critical points in more detail, it is customary to calculate the second derivatives of the ϵ spectra, which removes the nonresonant background and amplifies the singularities. In the vicinity of the critical points, we used a two-dimensional analytical line shape[22]

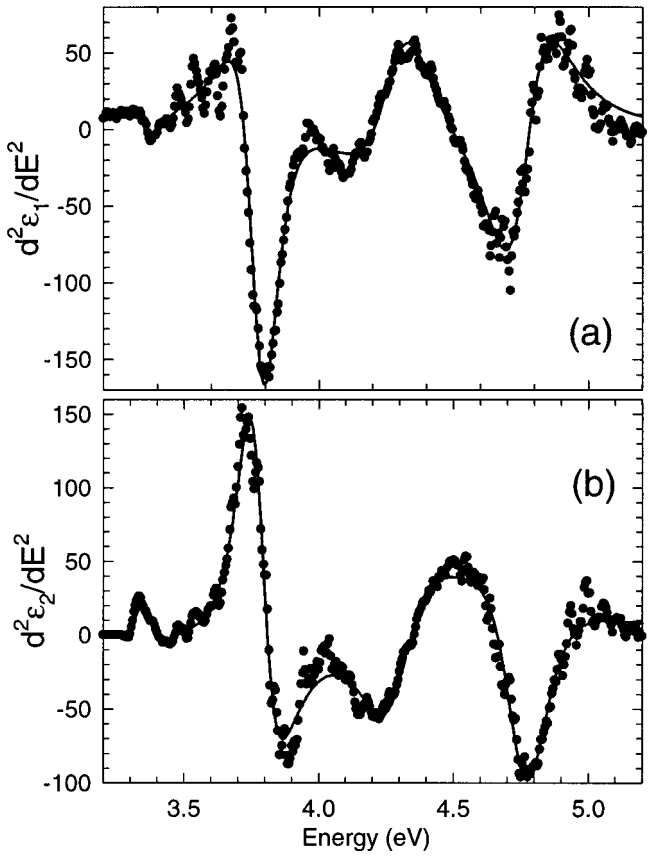

FIG. 4. Second derivative of ϵ vs photon energy in the range of critical points (symbols). The lines show the best fit to analytical line shapes with parameters given in Table II. The derivatives were calculated using the Savitzky–Golay algorithm with 20 points (in 5 meV steps) and fourth-order polynomials.

$$\epsilon(\hbar\omega)=A\exp(i\phi)\ln(\hbar\omega-E_g+i\Gamma), \tag{3}$$

based on an effective mass approximation for the band structure (with several valleys) and constant (**k** independent) dipole matrix elements, to describe our data. The critical-point parameters are the amplitude A, the energy gap E_g, the broadening Γ, and a phase angle ϕ describing many-body effects and interactions of several critical points fitted with one line shape.

For our critical-point analysis, we acquired data from 2 to 6.6 eV in 0.005 eV steps at a single angle of incidence (70°) without using the compensator, averaging over 400 analyzer cycles per data point to reduce the noise. Then, we determined ϵ in a wavelength-by-wavelength fit using the known roughness layer thickness (24 Å). The derivatives were calculated using the Savitzky–Golay algorithm. Next, we determined the critical-point parameters in comparison with the analytical line shapes in Eq. (3) using a least-squares minimization with the Marquardt–Levenberg algorithm.[23] Our results are shown in Fig. 4 and Table II. Above the lowest

TABLE II. Critical-point parameters (energy E_g, amplitude A, broadening Γ, and phase angle ϕ) determined by fitting the data in Fig. 4 to the two-dimensional analytical line shapes in Eq. (3). The 90% confidence limits are in parentheses. A tentative assignment based on band structure calculations is given in the last column.

	E_g (eV)	Γ (eV)	A (1)	ϕ (°)	Theory (eV)	Assignment
E_1	3.2(1)	N/A	N/A	N/A	3.19	$\Gamma-R$
E_0	3.355(3)	0.058(3)	1.13(5)	113(5)	3.55	Γ
	3.778(1)	0.101(1)	17.17(7)	146(1)		Ti($3d$)
	4.291(2)	0.177(2)	11.1(1)	320(1)	4.1, 4.4	X or Γ
	4.760(1)	0.150(1)	15.9(1)	254(1)	5.4	X
	6.15	0.15	N/A	N/A	6.8	M
	7–9	N/A	N/A	N/A		Sr($5d$) and sp^*

indirect (3.2 eV) and direct (3.4 eV) band gaps, we find higher gaps at about 3.8, 4.3, and 4.8 eV. At even higher energies, there are structures at 6.2 and 7–9 eV, which could not be fitted due to limitations of our software. The broadenings of our critical points are between 60 and 180 meV, not unreasonable for a crystalline material in comparison with Si.[22]

D. Comparison with theory

The most difficult task in analyzing the dielectric function of a material is the assignment of the critical points to optical interband transitions at certain points of the Brillouin zone. Usually, this is done in comparison with band structure calculations. We have therefore calculated the electronic structure of $SrTiO_3$ within the local-density approximation (LDA) using a plane-wave basis set. We used a commercial pseudopotential code (CASTEP), employing a plane-wave energy cutoff of 900 eV, ultrasoft pseudopotentials,[24] and k-space integrations with 40 special points. In general, the good agreement of the early calculations by Mattheiss[25] with our results is remarkable. Similar calculations, focusing less on the optical properties, were also performed using first-principles pseudopotentials[26] and with the linear-muffin-tin-orbitals method.[27]

The crystal structure[25] of $SrTiO_3$ consists of a simple cubic Bravais lattice with a lattice constant of $a=3.905$ Å and one molecular unit per cell [see Fig. 5(a)]. The Ti atom is located at the origin (filled), the Sr atom at the corners (shaded), and the three oxygen atoms (white, all three equivalent, i.e., related by lattice symmetry operations) at the centers of the cube faces. The space group is O_h^1. The Ti and Sr sites have the full O_h symmetry, whereas the site symmetry of oxygen is D_{4h}, that of the face center.[28] The Brillouin zone (BZ) for this lattice is shown in Fig. 5(b). The electronic energies at some high-symmetry directions of the BZ are shown in Fig. 6. In this (uncorrected) band structure, the indirect band gap is only 1.8 eV, less than the experimental band gap of 3.2 eV. This is commonly found in LDA calculations. Table III shows the energies at points of high symmetry. In this table, all conduction band energies were shifted by 1.4 eV to reproduce the experimental band gap.

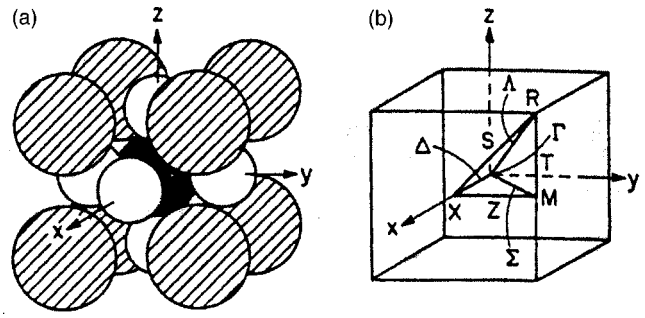

FIG. 5. (a) Unit cell for the perovskite compound $SrTiO_3$. Ti is filled, Sr is shaded, and O is white. (b) Brillouin zone for the simple cubic Bravis lattice.

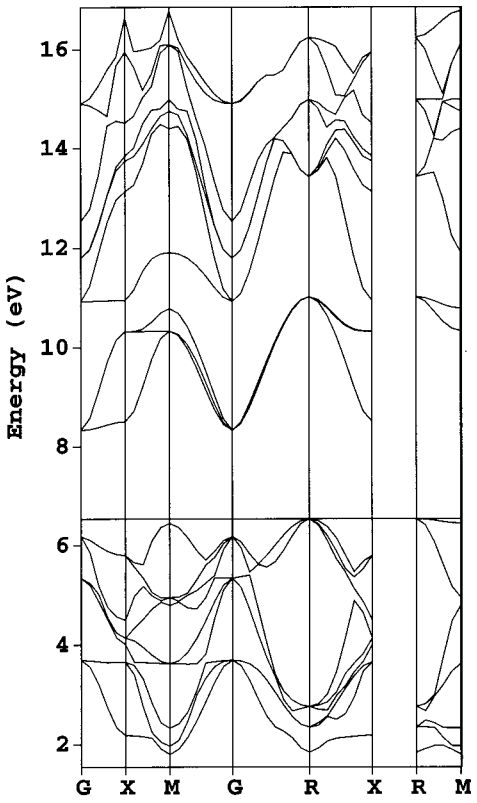

FIG. 6. Band structure of $SrTiO_3$ along some high-symmetry directions calculated using pseudopotentials with a plane-wave basis set within the LDA. The horizontal line shows the top of the valence band.

Our calculation includes the Ti($3s$) (band 1, −55.5 eV in our calculation, −62 eV in photoemission[29]), Sr($4s$) and Ti($3p$) (bands 2–5, −32.1 eV in our calculation, −37 eV in photoemission[29]), O($2s$) (bands 6–8, −16 eV in our calculation, −22 eV in photoemission), and Sr($4p$) (bands 9–11, −14 eV in our calculation, −20 eV in photoemission) core states, but these bands are at least 14 eV below the valence band maximum and therefore not given in Fig. 6 and Table III. The top nine valence bands (12–20) are primarily of O($2p$) character. (We do not find much charge near the Ti atoms.) They have a bandwidth of slightly less than 5 eV, in good agreement with photoemission results.[25,29] The spin-orbit splitting of the O($2p$) valence bands is very small.

TABLE III. Calculated energy levels at high-symmetry points. Valence band (top), conduction band (bottom). The conduction bands were shifted by 1.4 eV to overcome the LDA band gap problem. For degenerate states, the energy is only given for the state with the lowest band index (first column). The symmetry notations were taken from Ref. 25. The last line shows the symmetry of the *k* point (Ref. 33).

Band		Γ		*X*		*M*		*R*
12	Γ_{15}	−2.85	X_1	−4.36	M_3	−4.74	R_1	−4.70
13		⋯	$X_{5'}$	−2.88	M_1	−4.57	R_{12}	−4.19
14		⋯		⋯	M_2	−4.21		⋯
15	Γ_{25}	−1.19	$X_{4'}$	−2.53	M_5	−2.92	$R_{25'}$	−3.78
16		⋯	X_5	−2.40		⋯		⋯
17		⋯		⋯	$M_{4'}$	−1.74		⋯
18	Γ_{15}	−0.36	$X_{3'}$	−2.04	$M_{5'}$	−1.58	$R_{15'}$	0
19		⋯	$X_{5'}$	−0.74		⋯		⋯
20		⋯		⋯	M_4	−0.09		⋯
21	$\Gamma_{25'}$	3.19	X_3	3.37	M_5	5.19	$R_{25'}$	5.88
22		⋯	X_5	5.18		⋯		⋯
23		⋯		⋯	M_3	5.65		⋯
24	Γ_{12}	5.79	X_2	5.81	M_1	6.77	R_{15}	8.28
25		⋯	X_1	7.80	M_2	9.26		⋯
26	Γ_{12}	6.66	$X_{3'}$	8.61	M_1	9.61		⋯
27		⋯	$X_{4'}$	8.71	M_3	9.85	R_{12}	9.85
28	Γ_1	7.39	$X_{2'}$	9.38	M_5	10.96		⋯
29		9.76		10.81		⋯	$R_{12'}$	11.11
30		⋯		11.51	M_4	11.65		⋯
		O_h		D_{4h}		D_{4h}		O_h

The lowest three conduction bands (bands 21–23) are made up of Ti($3d$) bands. They have a bandwidth of 2.7 eV. The other two Ti($3d$) bands usually follow next at higher energies, but they mix with Sr($5d$) states and antibonding Ti, Sr, and O *s* and *p* orbitals at some points in the Brillouin zone to form the higher conduction bands. See also the augmented-plane-wave calculations of Mattheiss[25] using *ad hoc* potentials for a similar discussion.

We conclude that the lowest critical points observed in our optical spectra are primarily due to transitions from the O($2p$) valence bands to the Ti($3d$) conduction bands. Therefore, oxygen or titanium vacancies will reduce the amplitude of the peaks and the refractive index below the band gap much more than strontium vacancies. This will be important for the discussion of data on thin films. Interband transitions from the O($2p$) states to the Sr($5d$) states and the *sp*-antibonding orbitals start at 7 eV, where they give rise to a broad hump in our VUV ellipsometry data.

It can be seen from Fig. 6 and Table III that the valence band maximum is located at the *R* point, i.e., at the corner of the cubic BZ. The lowest conduction band state is located at the zone center Γ, which gives rise to an indirect band gap. There is a second local valence band maximum at Γ only 0.36 eV lower, which introduces a direct band edge at Γ with an energy of 3.55 eV, in good agreement with the experimentally observed direct gap at 3.4 eV.

Our calculations find the conduction-band minimum at Γ, but the *X* valley, favored as the global minimum in the early literature,[25,30–32] is only slightly (0.18 eV) higher. The symmetry of the conduction band minimum at Γ is similar to that of the valence band maximum in Si. There is a small spin-orbit splitting of about 38 meV, which leads to light, heavy, and split-off electron bands at Γ (see Mattheiss[25]). This splitting is less than the linewidths of our critical points, therefore the use of a nonrelativistic band structure calculation is justified.

The band structure of $SrTiO_3$ can be integrated to obtain the dielectric function, including the matrix elements of the dipole operator based on our calculated wave functions.[14] As noted before, the conduction band energies were shifted by 1.4 eV to correct the LDA band gap error. We also added a broadening of 0.2 eV to the calculated spectrum to account for the finite lifetime of the valence and conduction band states. The result of this calculation is shown by the solid line in Fig. 7 in comparison with the experimental data (dotted). Given the simple nature of our calculation, which ignores electron–hole interactions and describes the Ti and Sr *d* orbitals with plane waves (without taking into account the interaction between the *sp* continuum and localized states), the agreement is reasonable. After correcting the conduction band energies through a rigid shift, the onset of absorption and the peak at 4.2 eV are reproduced very well. The peaks in the measured ϵ_2 at 4.8 and 6.2 eV are also present in the calculation, but blueshifted by 0.5–1 eV. Finally, the calculation correctly finds a minimum of ϵ_2 near 7 eV and a peak at 8.5 eV due to Sr-related states. All peaks except those at the highest energies (where the lifetime broadening may be larger than 0.2 eV) have approximately the correct magnitude. ϵ_1 can be ignored in this discussion, since it is related to ϵ_2 by Kramers–Kronig transform.[14]

At high-symmetry points, group theory[33] can be used to determine if transitions between particular valence and conduction band states are allowed or forbidden. At the Γ and *R* points, the little group of the **k** vector is O_h, therefore the

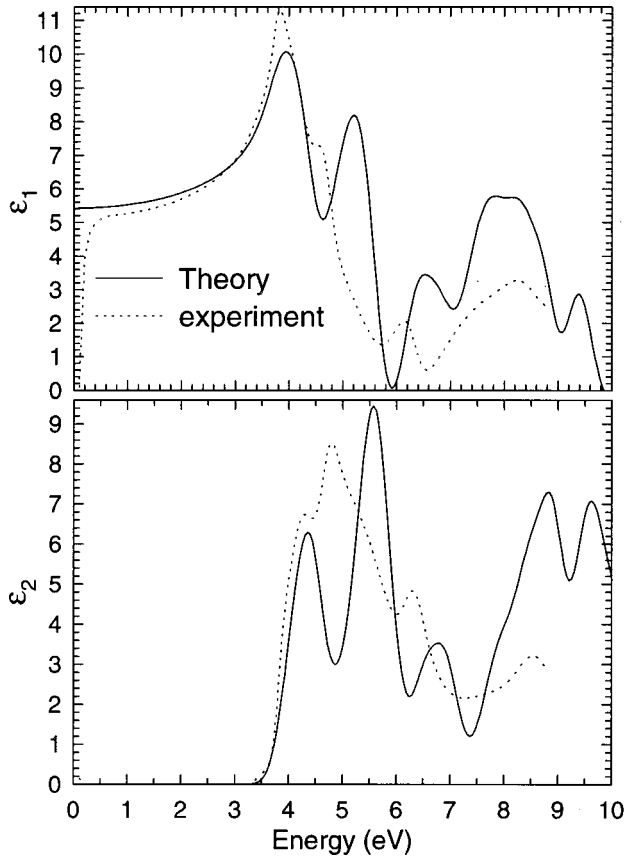

FIG. 7. Dielectric function of $SrTiO_3$ calculated from the LDA band structure in Fig. 6 (solid) in comparison with the experimental data from Fig. 3 (dotted). The conduction bands were shifted by 1.4 eV to overcome the LDA band gap problem and a lifetime broadening of 0.2 eV was added.

selection rules given by Bassani and co-workers[34] for the diamond structure can be applied. Of the possible interband transitions in Table III, only $\Gamma_{25}^{v} \rightarrow \Gamma_{1}^{c}$ is forbidden, the others at Γ are allowed. At the R point, many more transitions are forbidden. It is worth noting that all transitions from the $O(2p)$ valence bands to the lowest $R_{25'}$ conduction band (Ti related) are forbidden. This eliminates contributions to ϵ from the R point in our spectral range.

At the X point, there is a difference between the diamond and perovskite (simple cubic) selection rules caused by the absence of nonprimitive translations in $SrTiO_3$, which make all states at X doubly degenerate in the diamond structure.[33,34] To conserve parity, only transitions between even (unprimed) and odd (primed) states are allowed. At the X point, the dipole operator Γ_{15} splits into $X_{4'}$ and $X_{5'}$, which can be derived from the character tables.[35] The selection rules for optical interband transitions are obtained by reducing the tensor products of the small representations (see Table IV). For example, transitions from the highest (X_5') valence band to any of the Ti-related conduction bands (21–25) are allowed, but to the higher Sr-related conduction bands they are forbidden.

The selection rules at M are the same as those at X, since the little group is the same. At M, transitions from the highest valence band (M_4) to any of the conduction bands in Table III are forbidden by parity. Only transitions from the valence bands 17–19 $(M_{4'}, M_{5'}$ symmetry) are allowed.

TABLE IV. Selection rules for optical dipole transitions at the M and X points of the Brillouin zone.

M_i	M_1	M_2	M_3	M_4	M_5
$M_i \otimes M_{4'}$	$M_{4'}$	$M_{3'}$	$M_{2'}$	$M_{1'}$	$M_{5'}$
$M_i \otimes M_{5'}$	$M_{5'}$	$M_{5'}$	$M_{5'}$	$M_{5'}$	$M_{1'}+M_{2'}+M_{3'}+M_{4'}$

Based on these group-theoretical considerations and by considering only the contributions from high-symmetry points, we assign the origin of the critical points given by the last column in Table II. This ignores contributions from lines, areas, and volumes with lower symmetry, which are included in the calculation of ϵ in Fig. 7.

E. Lattice dynamics of bulk $SrTiO_3$

To study the lattice dynamics of bulk $SrTiO_3$, we measured the ellipsometric angles from 250 to 7450 cm^{-1} (0.031–924 meV) at four angles of incidence (60°, 65°, 70°, and 75°) using a commercial rotating-compensator FTIR ellipsometer described elsewhere.[36] Our discussion follows that of similar measurements performed by Humlíček,[37] but covers a larger spectral range. At 0.8 eV, our FTIR measurements yield $\epsilon_1 = 5.25$, in good agreement with measurements on the near-IR/visible/UV instrument of 5.23 at 0.8 eV, see above. $\langle \epsilon_2 \rangle$ is slightly positive (0.1) because of surface roughness. At 0.2 eV, ϵ_1 drops to 4.0 because of the influence of the lattice vibrations, but ϵ_2 is still very close to 0. See the low-energy region of Fig. 3.

The ellipsometric angles ψ and Δ in the region of the oxygen lattice vibrations (from 250 to 1000 cm^{-1}), taken at four different angles of incidence, are shown in Fig. 8. ψ is close to 45° over most of this range except for a drop near 500 cm^{-1}, where the oxygen-related transverse optical (TO) phonon is located.[38] By the same token, Δ drops from large values at 250 cm^{-1} to small values at 1000 cm^{-1} except for a derivative-like structure near 500 cm^{-1} due to the same lattice vibrations. To discuss these data, we express our ellipsometric angles as a pseudodielectric function (which is close to the dielectric function ϵ for this bulk sample with very little surface roughness). These data are shown in Fig. 9 (top). Since there is no dependence of ϵ on the angle of incidence, we only show data taken at 70°.

As mentioned above, $SrTiO_3$ is a perovskite crystal with cubic symmetry (see Fig. 5). The symmetries of the normal phonon modes at the Γ point can be derived using group-theoretical methods.[28] The Ba and Ti atoms give rise to one Γ_{15} mode each, the three oxygen atoms to two Γ_{15} modes and one Γ_{25} mode. Overall, subtracting one Γ_{15} acoustic mode, we expect three Γ_{15} modes (infrared active) and one Γ_{25} mode (silent). Since $SrTiO_3$ is an ionic crystal, each Γ_{15} mode splits into a TO and longitudinal optical (LO) pair. The energies of all these modes have been determined using hyper-Raman scattering.[38] The Sr-related modes have energies of 87 cm^{-1} (TO) and 179 cm^{-1} (LO) and the Ti-related

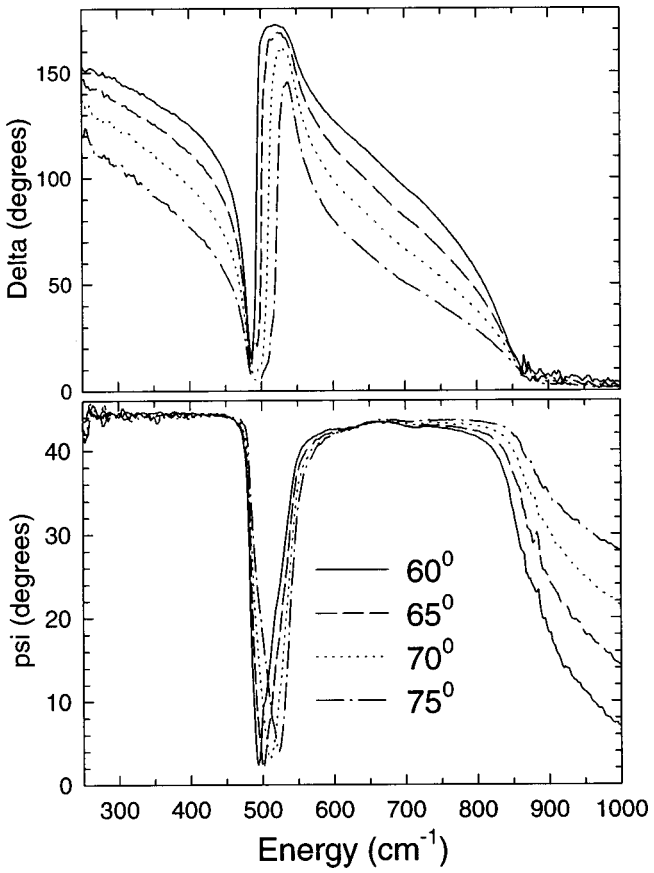

FIG. 8. Ellipsometric angles ψ and Δ at four angles of incidence in the infrared spectral region near the oxygen lattice vibrations.

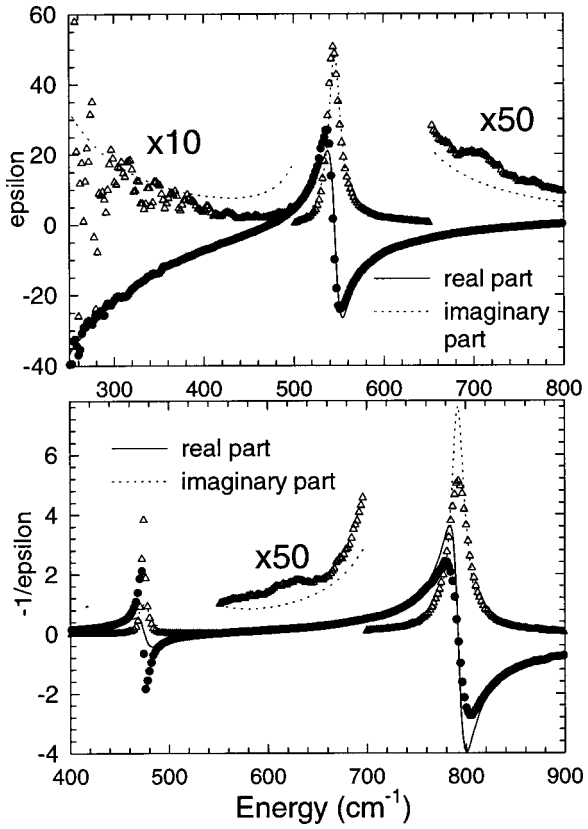

FIG. 9. Dielectric function ϵ (top) and loss function $-1/\epsilon$ (bottom) of bulk $SrTiO_3$, measured at 70° incidence (symbols) in the region of oxygen lattice vibrations, compared with a Lorentz oscillator model (lines).

modes have energies of 179 cm^{-1} (TO) and 472 cm^{-1} (LO). The silent Γ_{25} mode at 265 cm^{-1} does not influence our spectra. Finally, the oxygen-related modes are 542 cm^{-1} (TO) and 792 cm^{-1} (LO) according to the literature.[38]

Only the highest Γ_{15} mode is visible in our ϵ_2 spectra [see Fig. 9 (top)]. However, the decrease of ϵ_1 toward lower energies announces that one or more additional peaks occur below our spectral range. Therefore, our instrument cannot be used to measure ϵ_0 (i.e., the real part of ϵ at zero frequency), which is of primary technological interest, since its wavelength range is insufficient at low energies. We follow Gervais[17] and Humlíček[37] and use two Lorentz oscillators to model the dispersion of ϵ [see Eq. (2)]. Because of the limited range of our instrument, we ignore the weak Ti-related mode at 179 cm^{-1}. (Including it does not improve the agreement between data and model.) We fix the lower TO mode at $E_1 = 87\,\text{cm}^{-1} = 10.8\,\text{meV}$. All other parameters are fitted to best describe the spectrum of ϵ from 250 to 7450 cm^{-1}, although only a narrow range of the spectrum is shown in Fig. 9. The resulting parameters are: $\epsilon_\infty = 5.204$, $A_1 = 3.72 \times 10^{-2}\,\text{eV}^2$, $\Gamma_1 = 2\,\text{meV}$, $A_2 = 6.58 \times 10^{-3}\,\text{eV}^2$, and $\Gamma_2 = 2\,\text{meV}$. The oxygen-related TO phonon energy $E_2 = 67.7\,\text{meV} = 546\,\text{cm}^{-1}$ is in excellent agreement with the hyper-Raman data of Ref. 38. ϵ_1 crosses zero at 475 and 792 cm^{-1}. This is typically used as the criterion to define the LO phonon energy, again in good agreement with the literature.[38] The LO energies appear as peaks in the spectra when plotting the loss function $-1/\epsilon$ (see the bottom of Fig. 9). Our data also indicate additional structures at 700 cm^{-1} in ϵ and at 640 cm^{-1} in the loss function due to multiphonon absorption.

A comparison of the fit and the data shows that the experimental line shape is slightly asymmetric, there is more oscillator strength (absorption) at higher energies than on the low-energy side. This is also reflected in the real part of ϵ. When plotting the loss function, see the bottom of Fig. 9, we note that the calculated peak is higher than the data for the LO phonon at 792 cm^{-1} and lower for the LO phonon at 475 cm^{-1}, again an indication of the asymmetry. On the other hand, the LO peak positions are well matched between data and model. Such an asymmetric line shape is typically referred to as a Fano line shape and usually due to the interaction between a discrete state (the phonon) and a continuum, for example, free carriers.

In our case, since the $SrTiO_3$ crystal contains no free carriers, it is more likely that the asymmetry is caused by phonon–phonon interaction. Following Gervais,[17] we write ϵ based on a factorized form of the dielectric phonon response

$$\epsilon(E) = \epsilon_\infty \prod_{i=1}^{3} \frac{E_{i,\text{LO}}^2 - E^2 + i\Gamma_{i,\text{LO}}E}{E_{i,\text{TO}}^2 - E^2 + i\Gamma_{i,\text{TO}}E}. \quad (4)$$

This expression assigns different broadenings to the LO and

TO phonons. When the two broadenings are equal, the usual sum of Lorentzians is recovered.[39] Using Eq. (4) and by maintaining a 2:1 ratio of $\Gamma_{i,\mathrm{LO}}:\Gamma_{i,\mathrm{TO}}$, we are able to improve the agreement between our data and the model and introduce some asymmetry in the spectrum. However, measurements at longer wavelengths (below the Sr-related TO mode of 87 cm^{-1}) would be needed to clarify this point. We are not comfortable with fitting the broadening of a mode that is outside our spectral range. Measurements down to 50 cm^{-1} at the infrared synchrotron beamline in Brookhaven would be useful to study this material.[40] This has recently been done by Sirenko and co-workers.[41,42] The energies and broadenings of the low-energy phonon modes can also be studied using electric field-induced Raman scattering.[43]

III. OPTICAL PROPERTIES OF $SrTiO_3$ ON Si

After discussing the optical properties of bulk $SrTiO_3$, we proceed to those of thin $SrTiO_3$ films on various substrates. First, we note that the refractive index below the band gap of $SrTiO_3$ and $BaTiO_3$ films grown on MgO by molecular beam epitaxy is not noticeably different from the bulk.[7] However, there is a significant difference near the critical points,[7] which are broadened and have a lower amplitude. There are three possible explanations for this effect: (1) Due to a less perfect crystal structure in thin films than in the bulk, there is a scattering of the electron Bloch waves, which leads to a broadening of the critical points. This is often seen in micro-or polycrystalline semiconductors, such as Si or SiC. (2) There could be a difference in stoichiometry. Since the interband transitions originate from the $O(2p)$ valence band and end in the $Ti(3d)$ conduction band, oxygen or titanium vacancies (i.e., a change in stoichiometry) would certainly lead to a decrease of the critical-point amplitudes. (3) There could be other mechanisms for a charge transfer to Sr-related states, such as dislocations, grain boundaries[26] (in polycrystalline films), or interface states, which would reduce those amplitudes also. In similar studies on bulk $BaTiO_3$, a reduction of the refractive index in the surface region was observed after polishing, most likely due to a processing-induced damage at the surface.[44]

The $SrTiO_3$ films studied here were prepared by molecular beam epitaxy on Si(100) substrates as described elsewhere.[6] It is known that a few monolayers of $SrTiO_3$ on Si(100) can be grown without an amorphous interfacial layer.[2,6] However, in our thicker samples, we usually found an amorphous interfacial layer (10–40 Å thick) between the $SrTiO_3$ film and the Si substrate. This interfacial layer can be affected by the transmission electron microscope (TEM) sample preparation or by extended exposure to the electron beam, but careful studies of thinner films under similar conditions do not show such an interfacial layer, as noted earlier. There are several scenarios how this interfacial layer could be formed. One possibility is that, during the growth of thicker films, oxygen diffuses through the $SrTiO_3$ and reacts with the Si substrate (internal oxidation) (see Ref. 6). While the exact atomic structure and stoichiometry of this interfacial layer are not known to us, it certainly contains Si and O and could very well be a thin silicon oxide.

The $SrTiO_3$ film thicknesses were between 90 and 180 Å, measured by TEM and x-ray reflectivity. For all films, we determined the Sr/Ti ratio using x-ray fluorescence (XRF) using a methodology developed earlier[45] for $Ba_xSr_{1-x}TiO_3$ on Pt. For selected samples, the accuracy of this calibration using $Ba_xSr_{1-x}TiO_3$ XRF standards was confirmed using Rutherford backscattering and Auger spectrometry[3] (using a bulk $SrTiO_3$ standard). The films described here were usually slightly Sr rich and reduced, i.e., oxygen deficient, which could be overcome by postgrowth annealing in oxygen.[3]

The surface roughness of the films was measured by atomic force microscopy.[3,6] Typically, the rms roughness was between 1 and 5 Å, much less than for the bulk sample reported in Sec. II. Therefore, the $SrTiO_3$ film is atomically smooth and its roughness does not affect the ellipsometry analysis given below.

To verify the crystallinity and orientation of $SrTiO_3$ on Si, we measured θ–2θ x-ray diffraction (XRD) curves using a high-intensity Rigaku RU200-BH rotating-anode x-ray source and a DMAX-B goniometer, using an anode voltage of 50 kV, a beam current of 200 mA, and a divergence slit of 1°. Regardless of growth conditions, we only found the $SrTiO_3$ (100) and (200) lattice reflections.[3,6] There is no evidence for other crystalline phases in the film or a crystalline interfacial layer. The full width half maximum (FWHM) of the (200) lattice reflection usually was on the order of 1.3°, which corresponds to a film thickness of 65 Å, about half the film thickness measured by spectroscopic ellipsometry (see below). There could be some contribution to the x-ray diffraction linewidths due to lattice strain variations or dislocations, therefore the x-ray diffraction measurements underestimate the film thickness.

For all films on Si, we determined the ellipsometric angles from 0.74 to 6.6 eV, using the high-accuracy mode of the compensator as described above. The data were analyzed in a three-phase model (ambient/film/Si substrate), using the Herzinger–Johs parametric oscillator model to describe the $SrTiO_3$ film. For the thinner films (about 100 Å), there is some correlation between the thickness and the refractive index. Nevertheless, we feel that our measurements of these parameters can be trusted. This problem does not exist for films with 200 Å thickness or more. The penetration depth in bulk $SrTiO_3$ exceeds 110 Å for all wavelengths of our ellipsometer. Therefore, the $SrTiO_3$/Si interfacial layer will affect the data obtained in this three-phase model for all of our films, since the interfacial layer is not considered. For thinner films, the importance of the interfacial layer will be higher than for thicker films. In essence, this model reports an *average* dielectric function of the $SrTiO_3$ film and the interfacial layer. It is obvious that the interfacial layer thickness can be minimized by maximizing the refractive index below the band gap.

All films had a refractive index n at 632.8 nm (1.96 eV) that was significantly lower (1.85–2.23) than in bulk $SrTiO_3$ (2.39). Our best results (highest n) were obtained in slightly

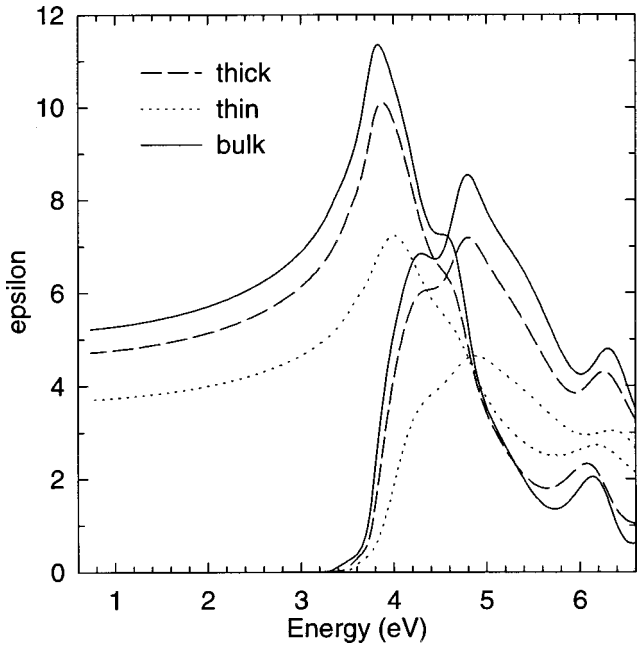

FIG. 10. Average dielectric functions of slightly Sr-rich $SrTiO_3$ films on Si determined within a three-phase (ambient/film/substrate) model. Due to the increasing importance of the interfacial layer between the film and the substrate, the average dielectric function is lower for a thinner film (110 Å, dotted) than for a thicker film (200 Å, dashed). The bulk $SrTiO_3$ dielectric function is shown by the solid line.

Sr-rich films with 200 Å thickness. For this stoichiometry, the refractive index decreases with decreasing thickness. If we stipulate that the amorphous interfacial layer has a refractive index similar to that of SiO_2 (1.4), which is considerably less than that of bulk $SrTiO_3$, then it is plausible that the average n for the film (interfacial layer plus $SrTiO_3$ film) decreases with decreasing film thickness, since the relative importance of the interfacial layer increases. To test this hypothesis, we attempted to describe the interfacial layer and $SrTiO_3$ as two different layers in the analysis of the ellipsometry data. We used our bulk $SrTiO_3$ data for the perovskite film and a Cauchy model (starting with the parameters of $SiO_2, n=1.4$, or $Si_3N_4, n=2.0$) for the amorphous interfacial layer. Unfortunately, none of these models led to a good description of the ellipsometric angles. A Bruggeman effective medium model with a mix of $SrTiO_3$ and SiO_2 to describe the film (or a mix of $SrTiO_3$ and Si to describe the interfacial layer) was also tested, but did not lead to a good agreement either. In summary, only a three-phase model (ambient/film/Si substrate) was found in good agreement with our ellipsometric angles. This model leads to an average dielectric function for the film, including the effects of the amorphous interfacial layer.

In Fig. 10, we show the average dielectric functions for two of our slightly Sr-rich $SrTiO_3$ films in comparison with bulk $SrTiO_3$. As mentioned above, ϵ_1 at 1.96 eV is lower than in the bulk for both films and decreases with decreasing thickness due to the increasing importance of the amorphous interfacial layer. However, the dielectric functions ϵ of the films cannot be represented by a scaled-down version of the bulk ϵ. In addition to the reduction of the amplitude of ϵ, there is a significant broadening of the critical points at 3.8, 4.3, 4.8, and 6.2 eV. This broadening could be due to the poorer crystallinity of the films compared to the bulk or due to confinement effects. We do not note a significant shift of the critical points or the band gap within the accuracy of our thin-film measurements. Furthermore, there is no significant absorption below the bulk band gap of 3.2 eV (i.e., no Urbach tail). The onset of strong absorption also remains about the same. (This can be seen better by normalizing ϵ_2 to the same peak amplitude for the three spectra than shown in Fig. 10.) Finally, while some of the reduction of ϵ in the films is due to the interfacial layer, there could also be a charge transfer to Sr-related states, which absorb at energies beyond our spectral range.

IV. OPTICAL PROPERTIES OF $SrTiO_3$ ON Pt

$SrTiO_3$ films were also prepared on Pt by chemical vapor deposition. For this study, a thermal oxide of 1000 Å thickness was produced on 200 mm Si (100) wafers. Then, 1000 Å thick Pt films (much less than the penetration depth of the light in our spectral range) were deposited at 450 °C by physical vapor deposition using high-purity targets, resulting in films with a rms surface roughness of less than 15 Å. The dielectric function of our Pt films prepared in this manner has been described elsewhere.[46] Their optical constants are quite different from values tabulated in the literature,[47] but consistent with ellipsometry measurements performed by others.[48] XRD measurements show that our Pt films are very strongly textured with the Pt (111) direction aligned with the growth direction. No XRD peaks other than Pt (111) and (222) plus the Si substrate peaks could be observed. The Pt grain size, determined from the FWHM of the Pt (111) peak, is about 350 Å. The FWHM of the Pt (111) rocking curves is about 3.7°, again indicating strong texture of the Pt films.

The $SrTiO_3$ lattice constant (3.905 Å) is very close to that of Pt (3.92 Å). Our best films are fully aligned with the Pt pseudosubstrate. Therefore, they cannot be studied using our XRD measurements. The texture of the $SrTiO_3$ films on Pt can be controlled by changing the deposition conditions. For those $SrTiO_3$ films with weaker texture, we observe $SrTiO_3$ (100) and (200) peaks in θ–2θ XRD scans. In this case, the average grain size of the $SrTiO_3$ grains aligned along (100) can be determined. It ranges from 100 to 200 Å. The $SrTiO_3$ films with smaller grain sizes also have weaker texture. The stoichiometry of the $SrTiO_3$ films was measured with x-ray fluorescence.[45] Some films were approximately stoichiometric, while others were significantly Ti rich (Sr/Ti ratio of 0.65 to 0.75).

The ellipsometric angles of twelve $SrTiO_3$ films on Pt prepared under different processing conditions were measured from 0.74 to 6.6 eV in the same manner as for $SrTiO_3$ on Si described above. The data were analyzed using a three-phase model (ambient/$SrTiO_3$/Pt), neglecting the small amount of surface roughness. The optical constants of the $SrTiO_3$ were again described using the Herzinger–Johs parametric oscillator model, ensuring Kramers–Kronig consis-

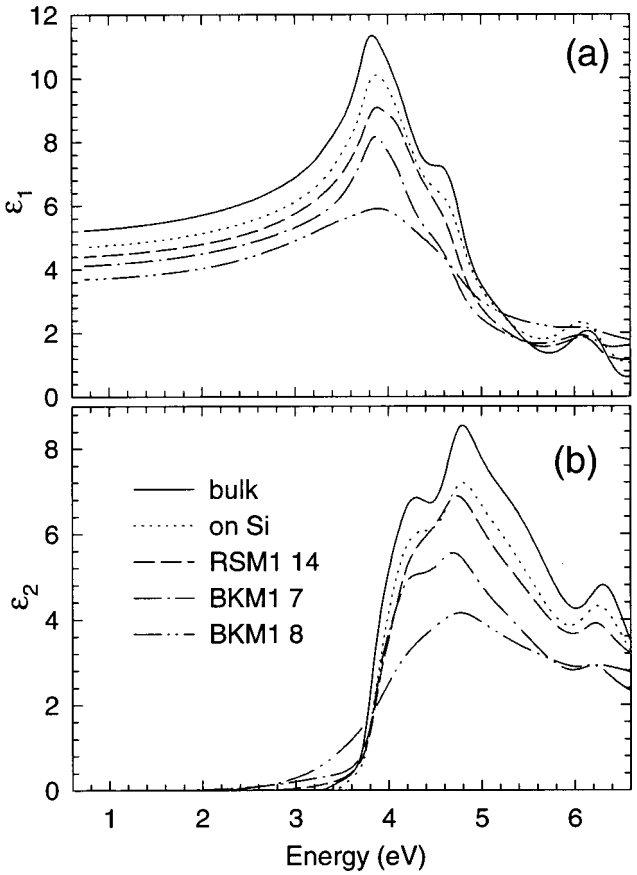

FIG. 11. Dielectric functions of polycrystalline $SrTiO_3$ films on Pt, about 230–280 Å thick, grown under different processing conditions (dashed, dot-dashed, double dot-dashed). The bulk $SrTiO_3$ dielectric function is shown by the solid line, that of the thick film on Si (see Fig. 10) by the dotted line.

tency of the optical constants while, at the same time, allowing a high degree of freedom for the dispersion of the optical constants. The film thicknesses were found to be between 210 and 280 Å. (For some films, the thicknesses were also confirmed by cross-sectional transmission electron microscopy.) The resulting (fitted) dielectric functions of the $SrTiO_3$ films on Pt are shown in Fig. 11. For comparison, we also show ϵ for bulk $SrTiO_3$ from Fig. 3 (solid) and for the thick $SrTiO_3$ film on Si from Fig. 10 (dotted).

For all films on Pt, we noticed a lower refractive index at 1.96 eV than for the thickest film on Si described earlier. The amplitudes of the critical points are also lower in the films on Pt. The films on Pt seem to have some absorption below the direct band gap (between 2.5 and 3.5 eV) indicating an Urbach tail. It is possible that this is an artifact of our data analysis, since such small values of ϵ_2 are difficult to measure for such thin films. However, since the $SrTiO_3$ films on Pt are grown at relatively low oxygen partial pressures, it is likely that they are reduced, i.e., oxygen-deficient. Linear-muffin-tin-orbital band structure calculations by Shanthi and Sarma[49] predict that oxygen vacancies act as shallow donors and dope $SrTiO_3$ with electrons. Vacancy clustering distorts the bottom of the conduction band and forms a distinct band tail in their calculations,[49] which is consistent with our experimental observations. The oxygen–vacancy related disorder also broadens the optical phonons,[50] which we discuss below.

The largest n at 1.96 eV is shown by a film that is significantly Ti rich (dashed line, Sr/Ti ratio of 0.75). This film shows an ϵ not too different from that of a stoichiometric film on Si with similar thickness (dotted). Based on our theoretical results, it is not too surprising that excess Ti (or lack of Sr) does not affect ϵ too much, since the interband transitions contributing to ϵ in our spectral range originate at the $O(2p)$ valence band and end in the $Ti(3d)$ conduction band. Sr-related states do not contribute to ϵ shown in Fig. 11.

The dot-dashed and double dot-dashed lines in Fig. 11 show ϵ for approximately stoichiometric $SrTiO_3$ films on Pt. Film number 7 (dot-dashed) is not visible in XRD because of perfect alignment with the Pt pseudosubstrate. Therefore, it is expected to have excellent crystallinity. This is also expressed in its dielectric function. All expected critical points are clearly visible, though at a lower amplitude than in the bulk or in the thick film on Si. Film number 8 (double-dot dashed) shows a strong and broad $SrTiO_3$ (200) XRD peak, indicating poor texture and a grain size of only 100 Å. The poor crystallinity expresses itself in a significant broadening of the critical points and a very strong Urbach tail below the band gap. This film also has the lowest refractive index at 1.96 eV of all films studied on Si and Pt with similar thickness.

To study the lattice dynamics of the $SrTiO_3$ films on Pt, we performed reflection absorption spectroscopy.[51] We measured the reflected intensity of the $SrTiO_3$ film on Pt (called R) and also the reflected intensity of the Pt pseudosubstrate R_0. Then, we calculate the quantity

$$1-\frac{R}{R_0}, \tag{5}$$

which should be equal to the optical density αd (where d is the film thickness) times a constant.[51] During these measurements, the angle of incidence was about 45° and the polarization state was not well defined, but the *s*-polarized component is expected to contribute very little to this signal.[51] A typical spectrum for a 225 Å thick film with a Sr/Ti ratio of 0.8, a refractive index of 2.20 at 1.96 eV, and good crystallinity is shown in Fig. 12. We observe two peaks approximately at the energies of the Ti- and O-related LO frequencies. There is no structure at the corresponding O-related TO frequency. This is a manifestation of the Berreman effect describing the infrared reflection response of a thin insulator on a metal, such as LiF on Ag.[52]

To compare these experiments with a model, we calculate the reflection absorption signal in Eq. (5) using our ellipsometry data analysis program.[53] We chose a polarization of 45° relative to the plane of incidence to see the effects of both *s*- and *p*-polarized beams. Since we do not have infrared ellipsometry data for the infrared dielectric function of Pt, we choose a Drude model for a typical metal with a plasma frequency of 13 eV and a broadening of 0.3 eV. The $SrTiO_3$ film is described with the same lattice dynamics model (sum

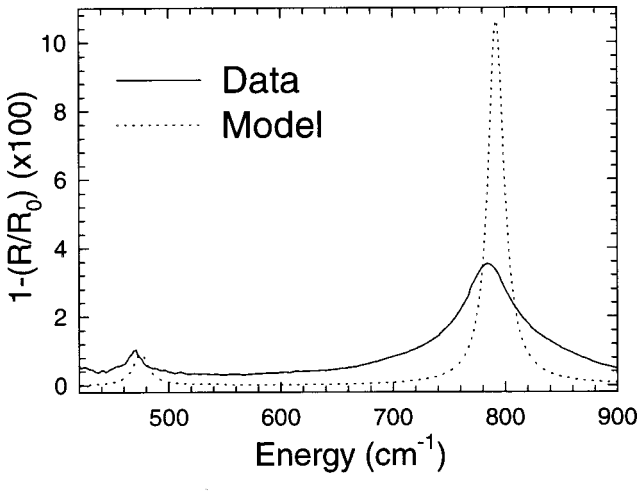

FIG. 12. Reflection–absorption spectrum (solid) of a $SrTiO_3$ film on Pt. Because of the Berreman effect, peaks at the LO phonon energies appear in this spectrum. The dashed line shows the spectrum calculated from our lattice-dynamical model for bulk $SrTiO_3$.

of two Lorentz oscillators) as in the bulk, see above. These data are shown by the dashed line in Fig. 12.

Comparing our experimental data with the model, we note that there are strong peaks in the signal due to the LO phonons. However, the LO energies are redshifted in the data compared to the model. Also, the amplitude of the LO peak at 475 cm^{-1} is approximately correct, whereas that of the peak at 792 cm^{-1} is overestimated by the model. This is not surprising in view of the bulk ellipsometry data in Fig. 9, where the LO phonon amplitudes are not correct either. However, in $SrTiO_3$ on Pt, the 792 cm^{-1} peak is broadened even more than in the bulk. The redshift and broadening compared to the bulk observed here is in contrast to infrared absorption work[50] in highly reduced $SrTiO_3$, where a blueshift and a broadening of the TO modes were observed. It is possible, though, that the TO and LO phonon shifts due to electron doping (caused by oxygen vacancies) could have different signs. The doping could screen the internal electric fields and thus change the TO–LO phonon splittings, resulting in hardening of one and softening of the other.

However, the LO redshift and TO blueshift observed in reduced $SrTiO_3$ are in contrast with the expected behavior resulting from the screening of the lattice vibrations by free electrons. In *n*-type GaAs, for example, the screening increases the LO energy and leaves the TO energy unchanged.[54] Therefore, the effects observed in $SrTiO_3$ have to be more subtle. For example, the changes of the phonon energies could also be affected by the local relaxation accompanying the oxygen vacancies.

It would be interesting the confirm our reflection–absorption spectroscopy results with infrared ellipsometry measurements, which are expected to be more sensitive, since they measure both the amplitude ratio and the relative phase of the *p*- and *s*-polarized beams.

V. CONCLUSION

We have performed extensive ellipsometry measurements over a broad spectral range to study the electronic structure, particularly the critical points, and the lattice dynamics of bulk $SrTiO_3$, in comparison with *ab initio* band structure calculations. We apply our understanding of the bulk to thin films on Si and Pt. In $SrTiO_3$ on Si, we observe a much lower refractive index below the band gap and a reduction of the critical-point amplitudes (but no shifts), particularly in thin films. Most likely, this is due to the amorphous interfacial layer between the Si substrate and the MBE-grown $SiTiO_3$ film. In $SrTiO_3$ on Pt, there is also a reduction of the low-energy refractive index, an amplitude reduction, and a broadening of the critical points, most likely due to a lower crystallinity (as in microcrystalline Si or SiC) combined with a charge transfer to Sr-related states at grain boundaries. We also observe a softening and an amplitude reduction of the LO phonons in $SrTiO_3$ on Pt in reflection–absorption measurements, which we attribute to oxygen vacancies in our films based on the growth conditions. Maximizing the crystallinity is likely to result in better electrical properties, i.e., higher resistivity and lower leakage currents through grain boundaries.

ACKNOWLEDGMENTS

The authors are grateful to C. M. Herzinger for providing the critical-point software and to Matthew Kim for supplying the $SrTiO_3$ bulk crystal. We also acknowledge stimulating discussions with Professor Josef Humlíček.

[1]Throughout this article, we follow the usual notation of lattice dynamics and call the dc dielectric constant ϵ_0, not to be confused with the permittivity of free space. The engineering literature refers to the same quantity as the relative permittivity with the symbol *k*, not to be confused with the extinction coefficient. $SrTiO_3$ is thus called a high-*k* material. Strictly speaking, ϵ_0 or *k* is not really a constant, but depends on the conditions of electrical measurements, such as the amplitude and frequency of the applied electric field, extrinsic properties such as interface states, and the thickness of the film.
[2]R. A. McKee, F. J. Walker, and M. F. Chisholm, Phys. Rev. Lett. **81**, 3014 (1998).
[3]Z. Yu *et al.*, Mater. Res. Soc. Symp. Proc. **567**, 427 (1999).
[4]Z. Yu *et al.*, J. Vac. Sci. Technol. B (in press).
[5]K. Eisenbeiser *et al.*, Appl. Phys. Lett. (in press).
[6]J. Ramdani *et al.*, Appl. Surf. Sci. (in press).
[7]G. E. Jellison, L. A. Boatner, D. H. Lowndes, R. A. McKee, and M. Godbole, Appl. Opt. **33**, 6053 (1994).
[8]G. E. Jellison, Opt. Mater. **1**, 41 (1992).
[9]G. E. Jellison and F. A. Modine, Appl. Opt. **29**, 959 (1990).
[10]H. G. Tompkins and W. A. McGahan, *Spectroscopic Ellipsometry and Reflectometry* (Wiley, New York, 1999).
[11]C. M. Herzinger and B. D. Johs, U.S. Patent No. 5 796 983 (18 August 1998).
[12]N. Sata, M. Ishigame, and S. Shin, Solid State Ionics **86–88**, 629 (1996).
[13]M. Cardona, Phys. Rev. **140**, A651 (1965).
[14]P. Y. Yu and M. Cardona, *Fundamentals of Semiconductors* (Springer, Berlin, 1996).
[15]M. Capizzi and A. Frova, Phys. Rev. Lett. **25**, 1298 (1970); Nuovo Cimento **5**, 181 (1971).
[16]K. W. Blazey, Phys. Rev. Lett. **27**, 146 (1971).
[17]F. Gervais, in *Handbook of Optical Constants*, edited by E. D. Palik (Academic, Boston, 1991), Vol. 2, p. 1035.
[18]J. L. Servoin, Y. Luspin, and F. Gervais, Phys. Rev. B **22**, 5501 (1980).

[19]D. Bäuerle, W. Braun, V. Saile, G. Sprüssel, and E. E. Koch, Z. Phys. B **29**, 179 (1978).
[20]G. E. Jellison, F. A. Modine, P. Doshi, and A. Rohatgi, Thin Solid Films **313–314**, 193 (1998).
[21]F. Urbach, Phys. Rev. **92**, 1324 (1953).
[22]P. Lautenschlager, M. Garriga, L. Viña, and M. Cardona, Phys. Rev. B **36**, 4821 (1987).
[23]J. W. Garland, C. Kim, H. Abad, and P. M. Raccah, Phys. Rev. B **41**, 7602 (1990).
[24]M. C. Payne, M. P. Teter, D. C. Allan, T. A. Arias, and J. D. Joannopoulos, Rev. Mod. Phys. **64**, 1045 (1992).
[25]L. F. Mattheiss, Phys. Rev. B **6**, 4718 (1972).
[26]S.-D. Mo, W. Y. Ching, M. F. Chisholm, and G. Duscher, Phys. Rev. B **60**, 2416 (1999); Y.-N. Xu, W. Y. Ching, and R. H. French, Ferroelectrics **111**, A23 (1990).
[27]F. M. F. de Groot, J. Faber, J. J. M. Michiels, M. T. Cryzyk, M. Abbate, and J. C. Fuggle, Phys. Rev. B **48**, 2074 (1993).
[28]D. L. Rousseau, R. P. Bauman, and S. P. S. Porto, J. Raman Spectrosc. **10**, 253 (1981).
[29]T. Higuchi, T. Tsukamoto, N. Sata, M. Ishigame, Y. Tezuka, and S. Shin, Phys. Rev. B **57**, 6978 (1998).
[30]A. H. Kahn and A. J. Leydendecker, Phys. Rev. **135**, A1321 (1964).
[31]H. P. R. Frederikse, W. R. Hosler, and W. R. Thurber, J. Phys. Soc. Jpn. **21**, 32 (1966).
[32]H. P. R. Frederikse, in *Electronic Structures in Solids*, edited by E. D. Haidemakis (Plenum, New York, 1969).
[33]G. F. Koster, Solid State Phys. **5**, 173 (1957).
[34]F. Bassani, G. P. Parravicini, and R. A. Ballinger, *Electronic States and Optical Transitions in Solids* (Pergamon, Oxford, 1975).
[35]L. P. Bouckaert, R. Smoluchowski, and E. Wigner, Phys. Rev. **50**, 58 (1936).
[36]B. Johs, J. A. Woollam, C. M. Herzinger, J. Hilfiker, R. Synowicki, and C. L. Bungay, Crit. Rev. Opt. Sci. Technol. **72**, 29 (1999).
[37]J. Humlíček, Ferroelectrics **176**, 221 (1996).
[38]V. N. Denisov, B. N. Mavrin, and V. B. Podobedov, Phys. Rep. **151**, 1 (1987).
[39]A. J. Sievers and J. B. Page, Phys. Rev. B **41**, 3455 (1990).
[40]A. Golnik, C. Bernhard, J. Humlíček, M. Kläser, and M. Cardona, Phys. Status Solidi B **215**, 553 (1999).
[41]A. A. Sirenko, C. Bernhard, A. Golnik, I. A. Akimov, A. M. Clark, J.-H. Hao, and X. X. Xi, Mater. Res. Soc. Symp. Proc. (in press).
[42]A. A. Sirenko, C. Bernhardt, A. Golnik, A. M. Clark, J. Hao, W. Si, and X. X. Xi, Nature (London) **404**, 373 (2000).
[43]I. A. Akimov, A. A. Sirenko, A. M. Clark, J.-H. Hao, and X. X. Xi, Phys. Rev. Lett. **84**, 4625 (2000).
[44]S. Trolier-McKinstry, R. E. Newnham, and K. Vedam, in *1990 IEEE 7th International Symposium on Applications of Ferroelectrics* (IEEE, New York, 1991), p. 650.
[45]T. Remmel, D. Werho, R. Liu, and P. Chu, in *Characterization and Metrology for ULSI Technology: 1998 International Conference*, edited by D. G. Seiler A. C. Diebold, W. M. Bullis, T. J. Shaffner, R. McDonald, and E. J. Walters (American Institute of Physics, Woodbury, NY, 1998).
[46]S. Zollner, Phys. Status Solidi A **177**, R7 (2000).
[47]D. W. Lynch and W. R. Hunter, in *Handbook of Optical Constants of Solids*, edited by E. D. Palik (Academic, New York, 1985), p. 275.
[48]L. Ley, T. Stark, M. Hundhausen, and H. Grünleitner, Mater. Res. Soc. Symp. Proc. (to be published).
[49]N. Shanthi and D. D. Sarma, Phys. Rev. B **57**, 2153 (1998).
[50]D. A. Crandles, B. Nicholas, C. Dreher, C. C. Homes, A. W. McConnell, B. P. Clayman, W. H. Gong, and J. E. Greedan, Phys. Rev. B **59**, 12842 (1999).
[51]H. G. Tompkins, in *Methods of Surface Analysis*, edited by A. W. Czanderna (Elsevier, Amsterdam, 1975), p. 445.
[52]J. Humlíček, Phys. Status Solidi B **215**, 155 (1999).
[53]J. A. Woollam Co., WVASE program (2000).
[54]A. Mooradian and A. L. McWhorter, Phys. Rev. Lett. **19**, 849 (1967).